

# Image Reconstruction from Events. Why learn it?

Zelin Zhang,  
TU Berlin

Anthony Yezzi\*  
Georgia Tech

Guillermo Gallego†  
TU Berlin, ECDF, SCIOI

## Abstract

Traditional cameras measure image intensity. Event cameras, by contrast, measure per-pixel temporal intensity changes asynchronously. Recovering intensity from events is a popular research topic since the reconstructed images inherit the high dynamic range (HDR) and high-speed properties of events; hence they can be used in many robotic vision applications and to generate slow-motion HDR videos. However, state-of-the-art methods tackle this problem by training an event-to-image recurrent neural network (RNN), which lacks explainability and is difficult to tune. In this work we show, for the first time, how tackling the joint problem of motion and intensity estimation leads us to model event-based image reconstruction as a linear inverse problem that can be solved without training an image reconstruction RNN. Instead, classical and learning-based image priors can be used to solve the problem and remove artifacts from the reconstructed images. The experiments show that the proposed approach generates images with visual quality on par with state-of-the-art methods despite only using data from a short time interval (i.e., without recurrent connections). Our method can also be used to improve the quality of images reconstructed by approaches that first estimate the image Laplacian; here our method can be interpreted as Poisson reconstruction guided by image priors.

## 1. Introduction

Event cameras are novel bio-inspired sensors that offer advantages over traditional frame-based cameras (high speed, high dynamic range (HDR), low power, etc.) [1, 2]. However they acquire visual data in the form of asynchronous per-pixel brightness changes, called “events”, instead of standard brightness images. We tackle the problem of image reconstruction from event-based data, i.e., recovering the brightness signal that caused the events. It is an interesting problem in itself and finds multiple applications: (i) it enables the creation of high-speed and/or HDR videos,

\*Georgia Institute of Technology, Atlanta, USA.

†Technische Universität Berlin, Einstein Center Digital Future, and Science of Intelligence Excellence Cluster, Berlin, Germany.

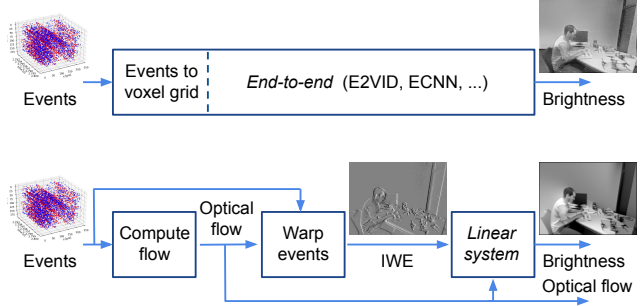


Figure 1. Overview of the proposed method (bottom) in comparison with state-of-the-art event-to-image RNNs (top). End-to-end image reconstruction methods can be replaced by an explainable system that recovers both optical flow and image brightness. We show that, given optical flow, image reconstruction is a linear problem in the unknown brightness. Hence many classical solvers and recent CNN-based ones can be used to estimate brightness.

(ii) if the reconstructed images are of sufficient quality they can be used as input to a large body of algorithms developed for traditional cameras. Hence, image reconstruction makes event data compatible with mainstream computer vision. Reconstructed images have applications from autonomous driving to smartphone applications for everyday use [3].

Image reconstruction is challenging because events are an unfamiliar representation of visual data, they depend on motion and contain a fair amount of noise and non-ideal effects (caused by pixel fabrication mismatch, the amount of incident light, sub-threshold transistor operation, etc.).

Recently, notable progress has been made in the topic. Early methods performed image reconstruction as a means to aid other estimation tasks, such as ego-motion estimation [4]. They were hand-crafted, proposing some a leaky integrator or filter that would perform some form of spatio-temporal smoothing and denoising [5, 6]. Nowadays, due to the outstanding capacity of artificial neural networks (ANNs) for pixel regression, state-of-the-art methods are deep-learning-based [7, 8]. They leverage large amounts of data in a supervised or unsupervised manner, via generative adversarial networks (GANs), to recover surprisingly high-quality image brightness from a voxelized representation of the event data, at a significantly higher computational cost compared to hand-crafted methods (Fig. 1, top).

However, these approaches suffer from several problems: (i) the resulting event-to-image ANNs are black boxes, relying on the networks to learn how to recover images from events; (ii) the ANNs suffer from artifacts and there is no easy way to tune them except for training with more data variation; (iii) the approaches focus only on recovering image brightness, but motion is as equally important to recover and both variables are firmly interconnected in the event data; (iv) events are sparse but they are converted into a voxelized representation for compatibility with ANNs, which causes a filling-in effect that requires considerable memory while most of the voxels may be empty; (v) some methods use a first-order event generation model, which inevitably introduces linearization errors.

Our work contributes to a new point of view on image reconstruction from event data. If one considers brightness and motion (i.e., optical flow) as equally important entangled variables in the event stream, the goal should be to estimate both (not just one of them) and to leverage existing *asymmetries* in the process. Specifically, we point out that, given optical flow, brightness estimation is a *linear problem*. Hence, (i) the difficult subproblem of the two is that of estimating accurate optical flow<sup>1</sup>, (ii) easier and more interpretable (explainable) methods than current ones shall be used for image reconstruction (Fig. 1, bottom). In particular, we leverage the fact that linear problems are extensively studied in science, and the corresponding solvers keep improving, benefiting from a growing body of work that exploits large image datasets. This naturally leads to lower dimensional, efficient intermediate representations. Additionally, the proposed image reconstruction method does not need ground truth (event,image) data pairs, which are required in state-of-the-art supervised learning approaches.

We evaluate the method on standard datasets and the experiments demonstrate that image reconstruction with the proposed technique (linear solver plus deep image priors) provides compelling results, on par with the state of the art in terms of quality, but without using any ground truth image and with notably better interpretability and flexibility.

In summary, our main **contributions** are:

- A novel formulation of the problem of image reconstruction from events, aided by optical flow, in the form of a linear system of equations directly in the unknown brightness image (Sec. 3.2).
- We propose a variety of solvers and regularizers, including recent deep denoisers, to solve the above problem, without using ground truth labels and using efficient input event representations (Sec. 3.4).
- Explainability: Our method combines physics (the event generation model used to derive the system of equations) and machine learning (for artifact removal through image denoising) (Secs. 3.2 and 3.4).
- Controlability: We can control the amount of regularization online, without retraining; just by changing a couple of hyperparameters.
- A natural extension of our method to perform image reconstruction and super-resolution (Sec. 3.5).
- We show that the same technique (linear constraints, inverse problem and CNN image priors) can be used to solve the image reconstruction problem in two different variants (Secs. 3.2 and 3.6). CNN image priors are combined with Poisson solvers to provide a non-linear (akin M-estimator) norm to guide the solution.
- A thorough evaluation on standard datasets and comparing with three state-of-the-art event-to-image RNN methods (Sec. 4).

## 2. Related Work

**Image brightness reconstruction from events.** Event cameras such as the DVS [10–13] are bio-inspired sensors that capture pixelwise *brightness changes*, called events, instead of brightness images. An event  $e_k \doteq (\mathbf{x}_k, t_k, p_k)$  is triggered as soon as the logarithmic brightness  $L$  at a pixel exceeds a preset contrast sensitivity  $C > 0$ ,

$$L(\mathbf{x}_k, t_k) - L(\mathbf{x}_k, t_k - \Delta t_k) = p_k C, \quad (1)$$

where  $\mathbf{x}_k \doteq (x_k, y_k)^\top$ ,  $t_k$  (with  $\mu\text{s}$  resolution) and polarity  $p_k \in \{+1, -1\}$  are the spatio-temporal coordinates and sign of the brightness change, respectively, and  $\Delta t_k$  is the time elapsed since the last event at the same pixel  $\mathbf{x}_k$ .

Image brightness  $L$  can be estimated from a stream of asynchronous events in many ways. Methods can be categorized into hand-crafted [4–6, 15–18] or learning-based [7, 8, 19–21]; sometimes they are both [22, 23], with submodules in each category. Some methods estimate the spatial brightness gradient ( $\nabla L$ ) first, as an intermediate quantity [4, 15–17, 22]. Then brightness is recovered by computing the Laplacian image and solving Poisson’s PDE [4, 17, 22] or a more robust version of it [16]. The first step may be bypassed, estimating the Laplacian image directly from events [23]. In [18] image brightness was obtained as the supporting variable of a costly, hand-crafted variational optimization problem whose primary goal was optical flow estimation. Many of the methods above require knowledge of the camera motion (pure rotation [4, 15], and/or depth [16, 17]). Only recently this requirement has been relaxed [5, 6, 18], achieving brightness reconstruction via temporal filtering [6] or temporal integration with manifold

<sup>1</sup>This admits analogies in other domains of computer vision, such as camera self-calibration [9]: given the plane at infinity, recovering the intrinsic parameters of the camera is a linear problem, too. Hence, finding the plane at infinity is the difficult (sub)task.

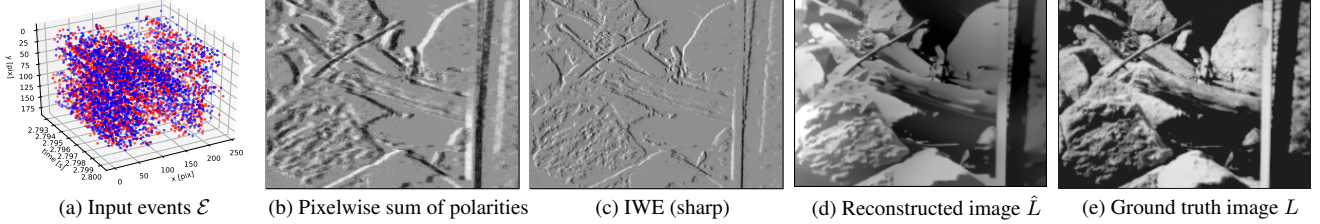


Figure 2. The events  $\mathcal{E}$  in (a) are motion-compensated using optical flow to create the image of warped events (IWE) (c). The sharp IWE approximates the  $x$ -derivative of the ground truth frame (e) better than the uncompensated image (b). Our method reconstructs brightness (d) from the IWE (c) by solving a linear system of equations with regularization. Texture details smaller than the contrast sensitivity  $C$  in (1) cannot be recovered since they do not trigger events. Data from *slider\_far* sequence in [14], consisting of rocks and tree-like textures.

denoising [5]. These hand-crafted approaches suffer from artifacts such as ghosting effects and bleeding edges.

**Deep learning event-to-image methods.** State-of-the-art methods let ANNs learn the mapping from events to brightness images. Events are typically converted into a dense voxelgrid representation and fed to modern ANNs. High quality results are obtained using supervised learning on recurrent neural networks (RNNs) trained on large amounts of synthetic data [7, 19, 20]. Unsupervised generative adversarial network (GAN) [8, 21, 24] and domain adaptation [25] approaches have been also investigated, but results are not as good. Recently, a self-supervised learning approach based on a linearized version of the event generation model (1) has been proposed in [26] to try to leverage large amounts of unlabeled event data for image reconstruction. It consists of two ANNs, one for optical flow estimation [27] and another one for image reconstruction, and the latter is trained using brightness constancy as a loss.

The above event-to-image deep learning methods are to a large extent black boxes, with a lot of effort spent not only on loss design and architecture search but also on dataset preparation [20, 24, 28] to train the ANNs and make them learn the desired transformation. Different from these methods, our approach does not train any event-to-image ANN. We pose the problem as image reconstruction aided by optical flow [26] and show that (1) leads to a *linear* system of equations. Several explainable methods are used to solve such a system. To achieve best results, we reuse state-of-the-art image denoising ANNs, without retraining.

### 3. Method

#### 3.1. 1D Example to build an intuition

To convey the main idea of our method let us consider the simple case of 1D motion (horizontally, along the  $x$  axis). For further simplicity, consider that the scene is planar and front-to-parallel with respect to the camera. Hence, all pixels on the image plane move with the same velocity  $\mathbf{u}$ .

Fig. 2 summarizes the main idea and steps of the method. Consider the set of events  $\mathcal{E} = \{e_k\}_{k=1}^{N_e}$  in a volume of the image plane (Fig. 2a). Since events are temporal bright-

ness changes, pixel-wise accumulation of the event polarities gives the brightness increment image in Fig. 2b. If the accumulation interval  $\Delta t = [t_1, t_{N_e}]$  is large, then this image is blurred. Instead, assuming the optical flow is known we may motion-compensate the events,  $\mathcal{E} \mapsto \mathcal{E}'$ , by displacing them to new pixel locations

$$\mathbf{x}'_k = \mathbf{x}_k - (t_k - t_{\text{ref}}) \mathbf{u} \quad (2)$$

(horizontally, in this case), where they will be aligned and produce a sharp Image of Warped Events (IWE) (Fig. 2c). This sharp image represents the strength of the moving edges in the scene [29], and it is entangled with the motion  $\mathbf{u}$ . The IWE resembles the  $x$ -derivative of the ground truth brightness frame. Such a spatial derivative is obtained from the brightness image using a finite difference operator  $D_x$ . In the simple case considered, we have:

$$D_x L \approx \text{IWE}(x, y) \quad (3)$$

where  $D_x L \doteq L(x+1, y) - L(x, y)$  is a 2-point finite difference approximation to the  $x$ -derivative over the pixel grid. More elaborate operators, like Sobel's, are applicable. The key ideas to notice are that each pixel of the IWE provides one equation (3) to recover the unknown brightness  $L$  and that equations are *linear* in  $L$ . Stacking (3) for all pixels, produces a *linear system of equations*  $D_x \ell = \text{vec}(\text{IWE})$  in the unknown  $\ell \doteq \text{vec}(L)$ . Hence, we reformulate the problem of image reconstruction as that of solving a linear system of equations. In the example, it is the problem of finding  $L$  whose  $x$ -derivative is the IWE. Thus one may study how well-posed the problem is, and test the large collection of linear solvers (GMRES, BiCGStab, etc.) to estimate  $L$ . If there are measurement errors in the equations, we may reformulate the problem as a least-squares one:

$$\min_{\ell} \|D_x \ell - \text{vec}(\text{IWE})\|_2. \quad (4)$$

Fig. 2d shows an example of a reconstructed brightness image  $L$  by solving the above system of equations with an additional regularization term. This is discussed next.

#### 3.2. Generalization to arbitrary Motions and Scenes

In the general case of arbitrary scene and motion we still follow the reasoning above, but with minor modifications.



Events  $\mathcal{E} \mapsto \mathcal{E}'$  are warped (2) according to an image velocity field that may change at each location,  $\mathbf{u}(\mathbf{x})$ . The resulting IWE is still sharp [29],

$$\text{IWE}(\mathbf{x}) \equiv \Delta L(\mathbf{x}) \doteq \sum_{k=1}^{N_e} C p_k \delta(\mathbf{x} - \mathbf{x}'_k), \quad (5)$$

but to account for different optical flow magnitudes  $\|\mathbf{u}(\mathbf{x})\| > 0$  (e.g., objects at different depths trigger a different number of events), we divide by the magnitude of the motion. This produces the normalized IWE (NIWE):

$$\Delta L'(\mathbf{x}) \doteq \Delta L(\mathbf{x}) / \|\mathbf{u}(\mathbf{x})\| \Delta t. \quad (6)$$

If  $\|\mathbf{u}(\mathbf{x})\| = 0$ , no events are triggered at pixel location  $\mathbf{x}$  and we set  $\Delta L'(\mathbf{x}) = 0$ . Assuming brightness constancy, the NIWE corresponds to the edge strength of the scene, i.e., instantaneous rate of brightness change in the optical flow direction at pixel  $\mathbf{x}$ :

$$\Delta L'(\mathbf{x}) \approx -\nabla L \cdot \hat{\mathbf{u}}(\mathbf{x}), \quad (7)$$

where  $\nabla L = (\partial_x L, \partial_y L)^\top$  is the spatial gradient and  $\hat{\mathbf{u}} = \mathbf{u}/\|\mathbf{u}\|$  is the unit vector in the direction of  $\mathbf{u}$ . The 1D example in Sec. 3.1 corresponds to the case  $\hat{\mathbf{u}}(\mathbf{x}) = -(1, 0)^\top$ , so that  $-\nabla L \cdot \hat{\mathbf{u}}(\mathbf{x}) = \partial_x L$ , and just like  $\partial_x L$  was discretized using a finite difference formula with a 1 pixel step over the pixel grid, we may also do so for  $\nabla L \cdot \hat{\mathbf{u}}(\mathbf{x})$ , leading to:

$$\Delta L'(\mathbf{x}) \approx L(\mathbf{x}) - L(\mathbf{x} + \hat{\mathbf{u}}(\mathbf{x})), \quad (8)$$

where  $L(\mathbf{x} + \hat{\mathbf{u}}(\mathbf{x}))$  can be computed by interpolation (e.g., bilinear interpolation). Stacking all equations (8), with the NIWE  $\mathbf{b} \doteq \Delta L'(\mathbf{x})$  computed from the input data (6), produces the anticipated *linear system of equations*

$$D\ell = \mathbf{b}, \quad (9)$$

where  $D\ell$  is a compact notation for the (directional derivative approximation given by the) right hand side of (8).

Notation: we use  $D$  to represent the operator acting on  $L$  or on its stacked version  $\ell$ . If  $L \in \mathbb{R}^{m \times n}$ ,  $\ell \in \mathbb{R}^{mn}$ , and  $D$  in  $D\ell$  is a sparse matrix of size  $mn \times mn$ , which can be constructed given the pixel-wise optical flow  $\hat{\mathbf{u}}(\mathbf{x})$ .

### 3.3. The Operator in the Linear System

One main challenge in solving the linear system (9) is that the operator  $D$  is not full rank. Hence, besides choosing a numerically good discretization for  $D$ , additional equations are needed to ensure that the problem is well posed.

Intuitively, in the 1D example of Sec. 3.1 we look for the image  $L$  whose  $x$ -derivative agrees with the data (the NIWE), and we know that inverting a derivative may be ill-posed. If  $D$  is discretized using the 2-point finite difference formula,  $DL(x, y) \approx L(x+1, y) - L(x, y)$ , each pixel of  $L$  is only strongly connected to one of its side neighbors, and so information in the linear solvers only propagates along

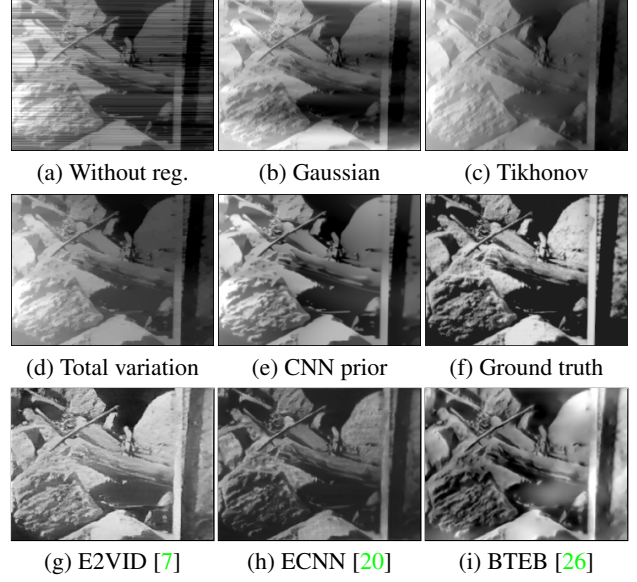


Figure 3. Image reconstruction using different regularization terms with increasing complexity (continued from Fig. 2). Solving the linear system (9) without regularization already captures most of the scene content (a), but the solution suffers from stream-like discretization artifacts along the optical flow lines. The regularization terms (b)-(e) mitigate the artifacts, thus improving image quality, by enforcing structural information in different ways. The last row shows results from state-of-the-art baselines (Sec. 4).

the rows of  $L$ . This causes streamline-like *artifacts* in the reconstructed image (Fig. 3a).

A simple way to mitigate these artifacts is to choose a better numerical discretization of  $D$  that encourages cross-talking (i.e., coupling) among more pixel neighbors. (Fig. 3b) shows the effect of replacing 2-point finite difference formula with Sobel’s 9-point formula, which couples each pixel to its 8 neighbors (matrix  $D$  is sparse and has at most 9 non-zero diagonals), thus encouraging smoothness of the solution in the direction perpendicular to the flow.

More advanced regularization techniques exist in the literature, such as Tikhonov regularization, total variation (TV), Beltrami, etc., as we discuss in the next section.

*Remark:* At border pixels, some optical flow vectors may point out of the image boundary. To tackle this issue, we set the optical flow and NIWE at border pixels to 0 so that both sides of (8) automatically agree. This operation, however, does not improve the rank-deficiency of matrix  $D$ .

### 3.4. Probabilistic Formulation and Priors

If we assume the measurement vector  $\mathbf{b}$  is corrupted by zero-mean Gaussian noise  $\mathbf{n}$  with variance  $\sigma^2$ , the observation process may be written as  $\mathbf{b} = D\ell + \mathbf{n}$ , yielding the conditional PDF  $p(\mathbf{b} | \ell) = \mathcal{N}(\mathbf{b}; D\ell, \sigma^2 \text{Id})$ .

The Maximum A Posteriori (MAP) estimate of the reconstructed brightness image  $\ell$  is given by  $\hat{\ell} =$



$\arg \max_{\ell} \log p(\mathbf{b} | \ell) + \log p(\ell)$ , where  $\log p(\ell)$  represents the prior on  $\ell$ . The estimation problem can be rewritten as

$$\hat{\ell} = \arg \min_{\ell} \frac{1}{2} \|\mathbf{b} - D\ell\|^2 + \lambda \mathcal{R}(\ell), \quad (10)$$

where the first term is the data fidelity term, and the second term is the regularization term.  $\lambda \geq 0$  is introduced to control the degree of regularization on the reconstructed image. The data term makes the estimation satisfy the observation process (i.e., the events), while the regularization term models structural information about the desired solution. Essentially we formulate the problem in a form that opens the door for the application of many regularizers, leveraging years of development in computer vision. Moreover, we can benefit from learning-based regularizers (i.e., image priors).

**Priors.** Generally, the regularizer in (10) can be classified into two categories: model-based priors and learning-based priors. In model-based regularization, the image is assumed to be smooth. Tikhonov regularization [30] penalizes the squared norm of the gradient of the solution, i.e.,  $\mathcal{R}(\ell) = \|\nabla \ell\|^2$ , where here the symbol  $\nabla$  represents the spatial gradient of  $L$ . Total variation (TV) regularization [31] penalizes the norm,  $\mathcal{R}(\ell) = \|\nabla \ell\|$ . Alternatively, the Beltrami regularization [32], which interpolates between the TV and Tikhonov, can be used as regularizer. The results of some of these regularizers are shown in Fig. 3.

Among the learning-based priors, convolutional neural network (CNN) image denoisers are a popular choice in recent research. To use a CNN image denoiser in the process of solving (10), we adopt the half quadratic splitting method (HQS) proposed in [33, 34]. To this end, we introduce an auxiliary variable  $\mathbf{z}$  that allows us to split the problem into two decoupled ones, and we couple them by increasing a penalty term linking  $\mathbf{z}$  to  $\ell$  as the iterations proceed. We replace (10) with

$$\hat{\ell} = \arg \min_{\ell, \mathbf{z}} \frac{1}{2} \|\mathbf{b} - D\ell\|^2 + \lambda \mathcal{R}(\ell) + \frac{\mu}{2} \|\mathbf{z} - \ell\|^2 \quad (11)$$

as  $\mu \rightarrow \infty$ . The problem is iteratively solved, alternating:

$$\begin{cases} \ell_k = \arg \min_{\ell} \|\mathbf{b} - D\ell\|^2 + \mu \|\ell - \mathbf{z}_{k-1}\|^2, & (12a) \\ \mathbf{z}_k = \arg \min_{\mathbf{z}} \frac{1}{2(\sqrt{\lambda/\mu})^2} \|\mathbf{z} - \ell_k\|^2 + \mathcal{R}(\mathbf{z}), & (12b) \end{cases}$$

where the data fidelity and regularization terms are decoupled into two separate optimization problems. Notably, (12a) admits a closed-form solution:

$$\ell_k = (D^T D + \mu \text{Id})^{-1} (D^T \mathbf{b} + \mu \mathbf{z}_{k-1}). \quad (13)$$

From a Bayesian estimation point of view, (12b) is an image denoising problem with additive Gaussian noise (of standard deviation  $\sqrt{\lambda/\mu}$ ). Theoretically, any Gaussian denoiser can be applied to (12b) to obtain a solution:

$$\mathbf{z}_k = \text{Denoiser}(\ell_k, \sqrt{\lambda/\mu}). \quad (14)$$

Since CNN image denoisers are shown to have a superior performance than other image denoisers, such as BM3D [35], we adopt CNN image denoisers to solve (14).

The effect of the alternating solver is that (12a) enforces the data fidelity equations while the denoiser (12b) pulls the solution towards the space of natural-looking images.

### 3.5. Image Reconstruction and Super-resolution

The proposed image reconstruction method can be naturally extended to enable super-resolution. The linear system (9) holds at any resolution, hence to achieve super-resolution we just need to provide the input NIWE  $\mathbf{b}$  and the operator  $D$  at the desired resolution. Operator  $D$  can be computed by optical flow interpolation. The NIWE is computed by warping events (2), which is done in floating point precision and using bilinear voting [36]. With enough warped events it is possible to provide a suitable NIWE at moderate upscaling factors (e.g.,  $\times 2 - \times 4$ ).

### 3.6. Image Reconstruction from its Laplacian

An alternative approach to reconstruct brightness from events is based on Poisson reconstruction [4, 17, 22, 23]. In the first step, events are used to estimate the Laplacian image,  $\mathcal{E} \mapsto \nabla^2 L$ , e.g., by means of an ANN [23]. In the second step, the Laplacian image is fed to a Poisson solver to recover image brightness. The key idea is that the first step is local whereas the second step is global. That is, events only need to affect nearby pixels to create the edgemap-like image  $\nabla^2 L$ , which can be achieved with an ANN (few layers, small receptive fields). The global step integrates the edgemap, filling in the brightness in regions with no events.

The relation between an image and its Laplacian can be written as a convolution  $\nabla^2 L(\mathbf{x}) = \kappa(\mathbf{x}) * L(\mathbf{x})$ , with the Laplacian kernel  $\kappa$ . In vectorized form, it is  $\mathbf{c} = \mathbf{k} \otimes \ell$ , where  $\mathbf{c} \doteq \text{vec}(\nabla^2 L)$ ,  $\mathbf{k}$  denotes the Laplacian kernel and  $\otimes$  denotes convolution. It is key to notice that this is, like (9), a *linear system of equations* in  $\ell$ . Hence, one may combine fast Poisson solvers with image priors to recover more perceptually appealing images. The optimization problem to recover  $\ell$  from the Laplacian  $\mathbf{c}$  becomes:

$$\hat{\ell} = \arg \min_{\ell} \frac{1}{2} \|\mathbf{c} - \mathbf{k} \otimes \ell\|^2 + \lambda \mathcal{R}(\ell). \quad (15)$$

This problem can be solved by the HQS method, with similar steps as those in Sec. 3.4. Equation (14) still applies, and if we assume the reconstructed image has periodic boundary conditions, the subproblem in the data fidelity term has closed-form solution (the analogue of (13)):

$$\ell_k = \mathcal{F}^{-1} \left( \frac{\overline{\mathcal{F}(\mathbf{k})} \mathcal{F}(\mathbf{c}) + \mu \mathcal{F}(\mathbf{z}_{k-1})}{\overline{\mathcal{F}(\mathbf{k})} \mathcal{F}(\mathbf{k}) + \mu} \right), \quad (16)$$

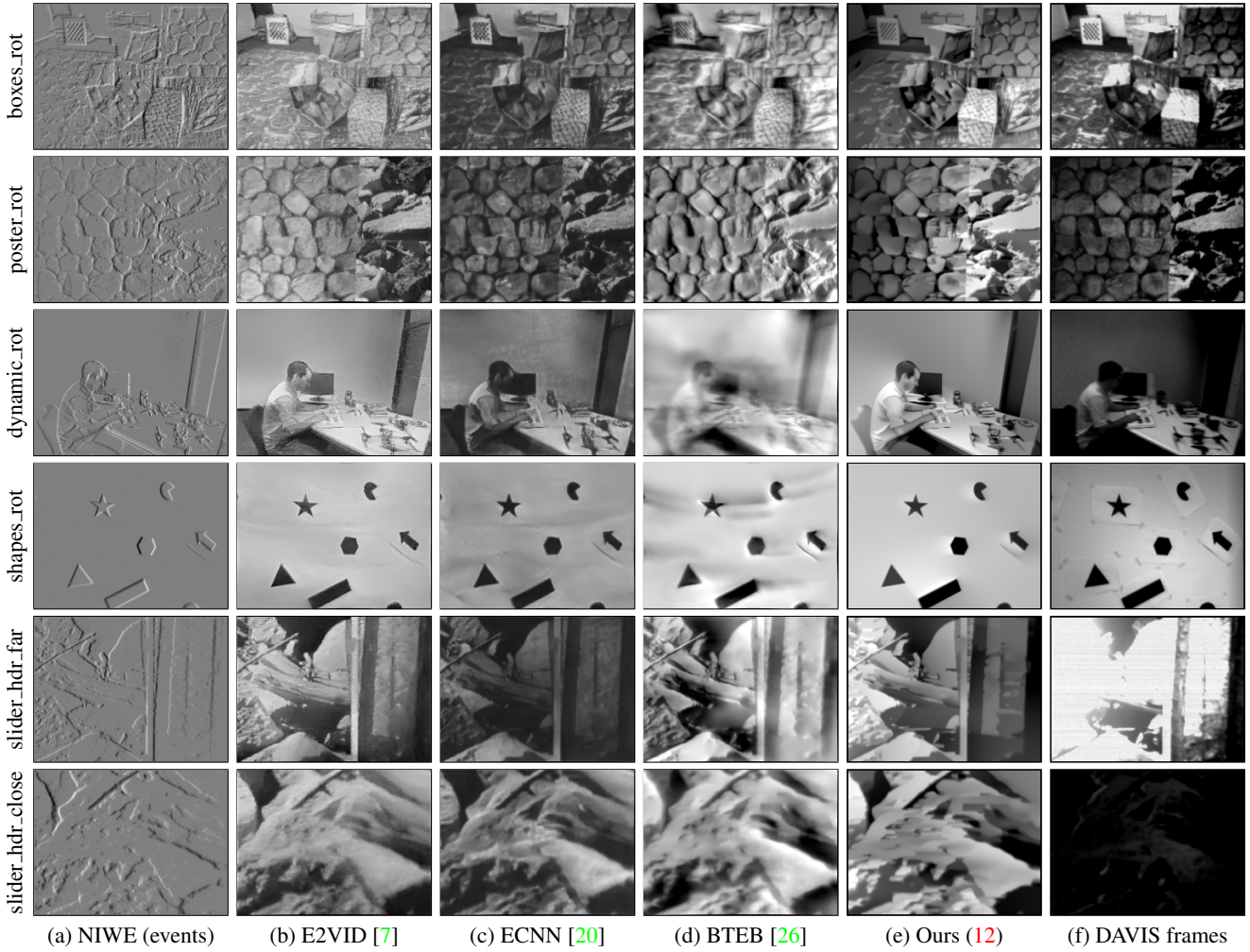


Figure 4. Qualitative comparison of our method with the state of the art on sequences from [14]. Histogram equalization is not used.

where  $\mathcal{F}(\cdot)$  represents the Discrete Fourier Transform (DFT),  $\mathcal{F}^{-1}(\cdot)$  is the inverse DFT, and  $\overline{\mathcal{F}(\cdot)}$  denotes the complex conjugate of  $\mathcal{F}(\cdot)$ . Without periodic boundary conditions, one may replace the DFT with the Discrete Cosine Transform (DCT) or the Discrete Sine Transform (DST) based on different symmetry assumptions.

## 4. Experiments

### 4.1. Image Quality Assessment

We evaluate the performance of our approaches on sequences from standard datasets [14, 37]. We compare with state-of-the-art image reconstruction methods [7, 20, 26]. E2VID [7] and ECNN [20] are event-to-image RNNs, trained in a supervised manner, with ground truth images. ECNN is an improved version of [7] trained on augmented data to reduce the sim-to-real gap. BTEB [26] comprises both an optical flow estimation CNN [27] and an image

reconstruction RNN, where the latter is trained in a self-supervised manner, without ground-truth images.

As is standard, we reconstruct images at the timestamps of the ground truth images (e.g., DAVIS frames) and compare in terms of mean square error (MSE), structural similarity (SSIM) [38] and perceptual similarity (LPIPS) [39]. We use the last 20k–50k events per IWE, depending on the amount of texture in the scene. The range of values of the regularizer weight is:  $\lambda \in [0.03, 0.05]$  for Tikh. and TV, and  $\lambda \in [0.19, 0.55]$  (see [33]) for the image prior denoiser.

Figure 4 shows qualitative results. As observed, our method (12) produces results on par with the state of the art. E2VID and ECNN produce high quality results, partly due to the large capacity of these RNNs to predict pixel intensities and because they are supervised methods. BTEB suffers from motion blur and “ghosting” artifacts (most noticeably in texture-less regions) [26]. Our method also suffers from some visual artifacts, but they are less pronounced

Sequence name	MSE ↓						SSIM ↑						LPIPS ↓					
	E2VID	ECNN	BTEB	Ours			E2VID	ECNN	BTEB	Ours			E2VID	ECNN	BTEB	Ours		
				Tikh.	TV	CNN				Tikh.	TV	CNN				Tikh.	TV	CNN
boxes_rotation	<b>0.046</b>	<u>0.049</u>	0.066	0.114	0.110	0.090	<u>0.489</u>	<b>0.535</b>	0.456	0.431	0.437	0.487	<u>0.389</u>	<b>0.370</b>	0.445	0.415	0.424	0.445
poster_rotation	<u>0.042</u>	<b>0.036</b>	0.063	0.133	0.128	0.075	<u>0.516</u>	<b>0.556</b>	0.456	0.384	0.396	0.507	<b>0.336</b>	<u>0.369</u>	0.459	0.437	0.446	0.439
dynamic_rotation	<u>0.074</u>	<b>0.073</b>	0.119	0.135	0.123	0.105	0.292	0.313	0.264	0.312	<u>0.334</u>	<b>0.355</b>	<u>0.487</u>	<b>0.478</b>	0.566	0.519	0.536	0.499
shapes_rotation	0.174	<u>0.103</u>	0.148	0.135	0.144	<b>0.090</b>	0.256	0.225	0.240	0.341	<u>0.398</u>	<b>0.419</b>	<b>0.541</b>	0.555	0.643	0.554	0.615	<u>0.546</u>
slider_far	<u>0.053</u>	<b>0.049</b>	0.086	0.127	0.101	0.069	0.408	<u>0.416</u>	0.374	0.318	0.379	<b>0.444</b>	<b>0.376</b>	<u>0.382</u>	0.446	0.443	0.444	0.450
slider_close	<b>0.026</b>	<u>0.026</u>	0.055	0.082	0.071	0.050	<u>0.411</u>	<b>0.451</b>	0.352	0.348	0.373	0.408	<u>0.500</u>	<b>0.498</b>	0.561	0.542	0.545	0.532
Average	<u>0.069</u>	<b>0.056</b>	0.090	0.121	0.113	0.080	0.395	<u>0.416</u>	0.357	0.356	0.386	<b>0.437</b>	<b>0.438</b>	<u>0.442</u>	0.520	0.485	0.502	0.485

Table 1. Quantitative comparison of our method with the state of the art on sequences from [14]. We report median values (since they are more robust to outliers than the mean) of MSE, SSIM and LPIPS quality metrics. Images are equalized before computing the metrics.

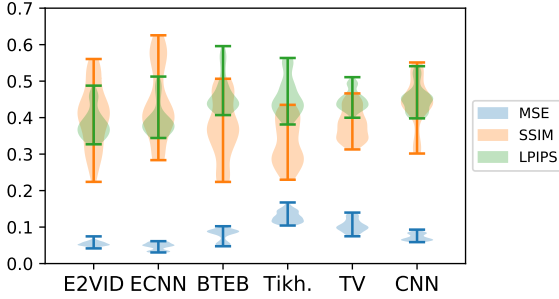


Figure 5. Distribution plots of the six methods in Tab. 1, on the slider\_far sequence [14].

than those of BTEB. The reconstructed images have a clean, smooth appearance, which is conferred by the image denoiser within the solver (12b). Our method fills with a smooth clean look the texture-less regions (we also observe this in the different variants presented in Fig. 3), whereas BTEB is reported to have limited extrapolation capacity of edge information. However, our regularizer tends to smooth fine-grained details as they are considered noise.

The last two rows of Fig. 4 show HDR results. In these sequences comparison is only qualitatively since ground truth images are not HDR. Our method is able to reconstruct high quality HDR images, on par with learning-based methods, and showing a smooth look, which can be controlled online via the regularizer weight.

Quantitative results using the above metrics for six different methods are provided in Tab. 1. The choice of evaluation metric and protocol plays a big role in the numbers. For example, our image prior method produces the best results in terms of SSIM, whereas E2VID and ECNN are better in other metrics. Despite not using ground truth images and not having recurrent connections to past events beyond the IWE, our three methods (Tikh., TV and CNN) produce results in line with the state of the art in reconstruction quality. Figure 5 plots the distribution of MSE, SSIM and LPIPS values for the six methods of a row of Tab. 1. Surprisingly, solutions as simple as classical Tikhonov or TV regularizers acting on a linear system of equations produce already sim-

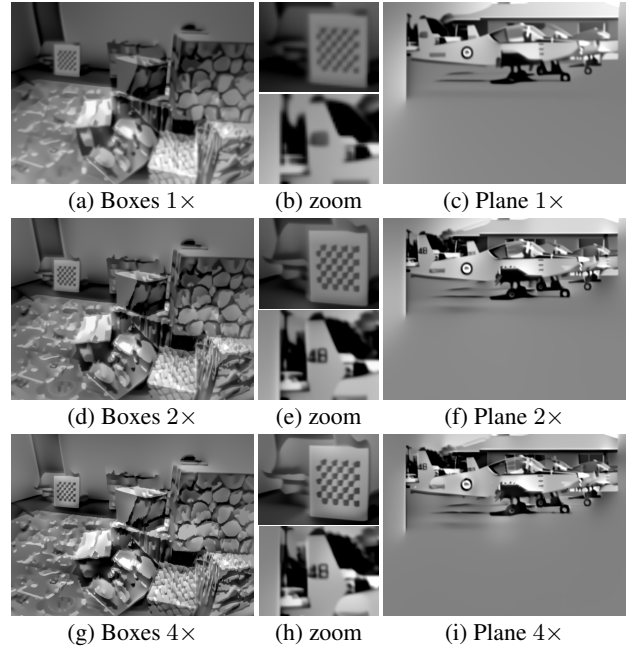


Figure 6. *Super-resolution*. Reconstructing and super-resolving brightness by factors of 2× and 4× in each spatial dimension. Details are best viewed by zooming in.

ilar quality results as complex learning-based approaches. The violin plots of the proposed regularizers follow monotonic trends in MSE and SSIM, but the trend is not clear in terms of LPIPS. Results highly depend on metrics.

## 4.2. Super-resolution

With super-resolution we basically convert part of the high temporal resolution of the event camera into spatial resolution. Figure 6 shows results on simultaneous brightness reconstruction and super-resolution (Sec. 3.5) on sample sequences from [14, 37]. Input resolutions (1×) are  $240 \times 180$  pixels for [14] (DAVIS camera) and  $304 \times 240$  pixels for [37] (ATIS camera). The super-resolved images have 2× and 4× more pixels in each dimension (i.e., about 1Mpixel). To build the IWE at resolutions 2×, 4× we slightly increased the number of events (less than doubled).



Sequence name	MSE ↓		SSIM ↑		LPIPS ↓	
	[23]	Ours (15)	[23]	Ours (15)	[23]	Ours (15)
brain	<b>0.008</b>	0.010	0.713	<b>0.739</b>	0.227	<b>0.211</b>
brain + noise	0.014	<b>0.013</b>	0.664	<b>0.692</b>	0.357	<b>0.276</b>
car	0.028	<b>0.024</b>	0.673	<b>0.694</b>	<b>0.360</b>	0.384
car + noise	0.037	<b>0.034</b>	0.619	<b>0.633</b>	<b>0.380</b>	0.430
chair	<b>0.057</b>	0.064	<b>0.831</b>	0.825	<b>0.272</b>	0.296
chair + noise	<b>0.036</b>	0.043	0.729	<b>0.722</b>	0.393	<b>0.359</b>

Table 2. Quantitative comparison. Reconstruction from Laplacian.

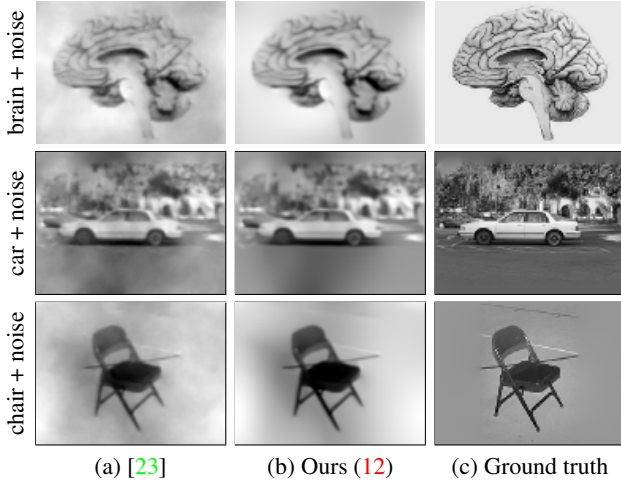
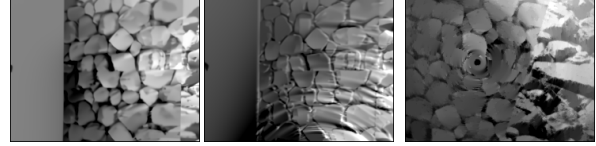


Figure 7. *Reconstruction using the Laplacian*. Results of reconstructing brightness using the method of Sec. 3.6.

There is a trade-off: using more events improves the SNR and fills in the super-resolved pixels of the IWE; however, it also increases the time spanned by the events, and motion compensation may not be effective assuming constant optical flow during that time span. In the images, we observe that increasing from  $1\times$  to  $2\times$  makes a big difference: at  $2\times$  we can read the number “48” on the fin of the plane. In the boxes scene, at  $2\times$  the checkerboard and the texture of the boxes become sharper. From  $2\times$  to  $4\times$  the improvement is not as striking: the checkerboard and the contours of the folded foam mattress behind it become sharper, but we cannot read the text below the plane’s fin. This may be difficult given the input spatial resolution.

### 4.3. Image Reconstruction via the Laplacian

Here we demonstrate the method of Sec. 3.6. First we use the ANN in [23] to predict the Laplacian image  $\mathbf{c}$  from the events. Then this image is passed to our solver (15). Tab. 2 and Fig. 7 report results, where we also add Gaussian noise to the Laplacian. The Laplacian is given in the range  $[-0.6, 0.6]$ , and the noise has  $\sigma = 0.02$ . Given the limited spatial input resolution of  $\mathbf{c}$  provided by the ANN ( $120 \times 90$  pixels), the differences between [23] and our method are most noticeable in the way they deal with noise. Our method yields higher contrast, sharper edges and



(a) Change of direction (b) Rotation artifact  
Figure 8. Failure cases

smoother homogeneous regions due to the CNN denoiser. Regarding Tab. 2, the differences are not as large and depend on the metric; our method is clearly better on SSIM.

### 4.4. Limitations

Our method is based on the assumption of known optical flow, like [26]. This allowed us to focus on reformulating the image reconstruction part as a linear inverse problem and propose efficient, explainable solvers. However, this is not a major problem since optical flow may be estimated by modern methods [26, 27, 40]. Here we used the most accurate optical flow available (given by ground truth camera motion) to explore the possibilities of the framework.

We use CNN image priors for regularization and to remove artifacts. While the majority of artifacts are removed, some remain (Fig. 8). For example, when the flow changes direction abruptly within an event packet, motion compensation with a single motion model may fail to give a good NIWE. Hence, two consecutively reconstructed images may change appearance dramatically (Fig. 8(a)-(b)). Another artifact that may arise is black or white spots (Fig. 8(c)), produced if the center of rotation lands in the middle of the image (no events in the NIWE). These artifacts are due to the fact that we do not explicitly model temporal consistency or recurrent connections. Future research could look into mitigating these artifacts via some temporal filtering.

Like other reconstruction methods, we only recover brightness based on moving edges. If the camera is stationary, this might lead to inconsistencies [26], which could be resolved by combining events and grayscale frames [6].

## 5. Conclusion

Instead of mainstream end-to-end brightness reconstruction from events based on RNNs, we have emphasized the framework of jointly estimating the two entangled quantities in the events: brightness and motion (optical flow). And we have shown how, using motion to generate images of warped events, brightness reconstruction is a linear problem, which we have tackled with classical regularizers and image priors. Beyond the particular results showing reconstruction quality in line with the state of the art, we believe our approach (linear equations plus image prior) is appealing because it unifies multiple problems, including super-resolution and reconstruction based on either first (NIWE) or second derivative (Laplacian) of brightness.

## A. Supplementary Material

### A.1. Additional quantitative results on [14]

Table 3 reports quantitative comparison of the reconstructed images on sequences from [14] without histogram equalization. Hence, it complements Table 1 in the main paper (results on equalized images). Equalizing the images makes the result of the comparison metrics more invariant to changes in average intensity level. For example, the SSIM metric comprises two parts: one that depends on the means and one that depends on the variances. Without histogram equalization, both terms contribute to the SSIM. However, with histogram equalization, the effect of the term that depends on the means is greatly reduced, and therefore the term that depends on the variances dominates the metric.

The changes in the mean intensity are also noticeable in the MSE metric. ECNN tends to produce dark images, like those of the DAVIS camera in [14], which often only span a 7-bit range of intensities (from 0 to 127). Hence, without histogram equalization ECNN tends to outperform other methods on these sequences just by producing darker images. With histogram equalization, E2VID and ECNN are best in terms of MSE (Tab. 1), but without it we see that ECNN is the top one and our image prior approach (CNN) is consistently the second best (Tab. 3). *Why?* Histogram equalization is a non-linear transformation that is not part of the event generation model (1). Hence, it is reasonable that our methods (Tikhonov, TV and CNN image prior), which aim at solving a system of equations based on (1), produce better evaluation values on metrics without image equalization than on metrics with image equalization. The established evaluation protocol [7, 20, 26] is somehow contradictory: we design estimators to solve some equations (i.e., based on (1)) and then we measure their goodness of fit using a different set of equations that are non-linearly related. In summary, the fact that the quantitative ranking / results highly depend on the metric and on the evaluation protocol (e.g., equalized vs. not equalized), tells us that one should be careful when taking these numbers as an “absolute truth” about the performance of the different methods tested.

### A.2. Additional results on N-Caltech 101 [37]

Figures 9 to 11 show qualitative results on the N-Caltech 101 dataset. The figures are complemented by Tab. 5. We aligned the images with respect to the ground truth using ECC (Enhanced Correlation Coefficient) maximization to be able to report quantitative results on the usual metrics (MSE, SSIM, LPIPS). This dataset comprises sequences of 300 ms, with 3 saccades of 100 ms each. In the tests, we leave the first saccade as initialization for RNN baseline methods [7, 20, 26], and compare the results in the middle of the 2nd saccade. In our method, we only use 60 ms of

data from the middle saccade.

Quantitatively we observe that the total variation (TV) regularizer produces very good results in all three metrics using unequalized images (Tab. 5), with the CNN image prior being a competitive option in terms of MSE and SSIM, and E2VID in terms of LPIPs. The performance of E2VID and ECNN improves if equalized images are used in the evaluation protocol. Qualitatively, we observe in Figs. 9 to 11 compelling high-quality reconstructed images by our TV and image-prior methods compared to the state of the art [7, 20, 26].

### A.3. Evolution of the solution with the iterations

Figure 12 shows the inner workings of the iterative solver (12) on sample sequences. We run the image-prior solver (12) for 16 iterations. In the figure we depict the evolution of the two variables  $\ell_k, \mathbf{z}_k$  as iterations proceed. They start far apart, but converge to each other with the iterations. The auxiliary variable  $\mathbf{z}_k$  starts as a very smooth and denoised version of the solution, and it achieves higher level of detail (less smoothing) with the iterations. The brightness image  $\ell_k$  starts with very fine details and also artifacts in the direction of the optical flow (e.g., Fig. 3a), and some of the details get lost along with the artifacts as it is denoised. In the alternating process, the iterative solver (12a) enforces the data fidelity equations while the denoiser (12b) pulls the solution towards satisfying structural constraints (i.e., in the space of natural-looking images).

### A.4. Motion Segmentation & Image Reconstruction

Additionally, we provide in Fig. 13 qualitative results on the combination of our method and motion segmentation. The motion segmentation methods in [41, 42] classify the events into different clusters according to similarity of motion. Each cluster has an associated IWE whose contrast is maximized with the events that belong to the cluster. Hence, we can use the IWEs and motion parameters obtained via motion segmentation as input to our method. As Fig. 13 shows, we can recover brightness of the foreground and the background separately (each one is represented by a different cluster, and therefore different IWE and motion parameters). The combination of event-based motion segmentation and image reconstruction has the effect of splitting a theoretically reconstructed image into its moving parts / components.

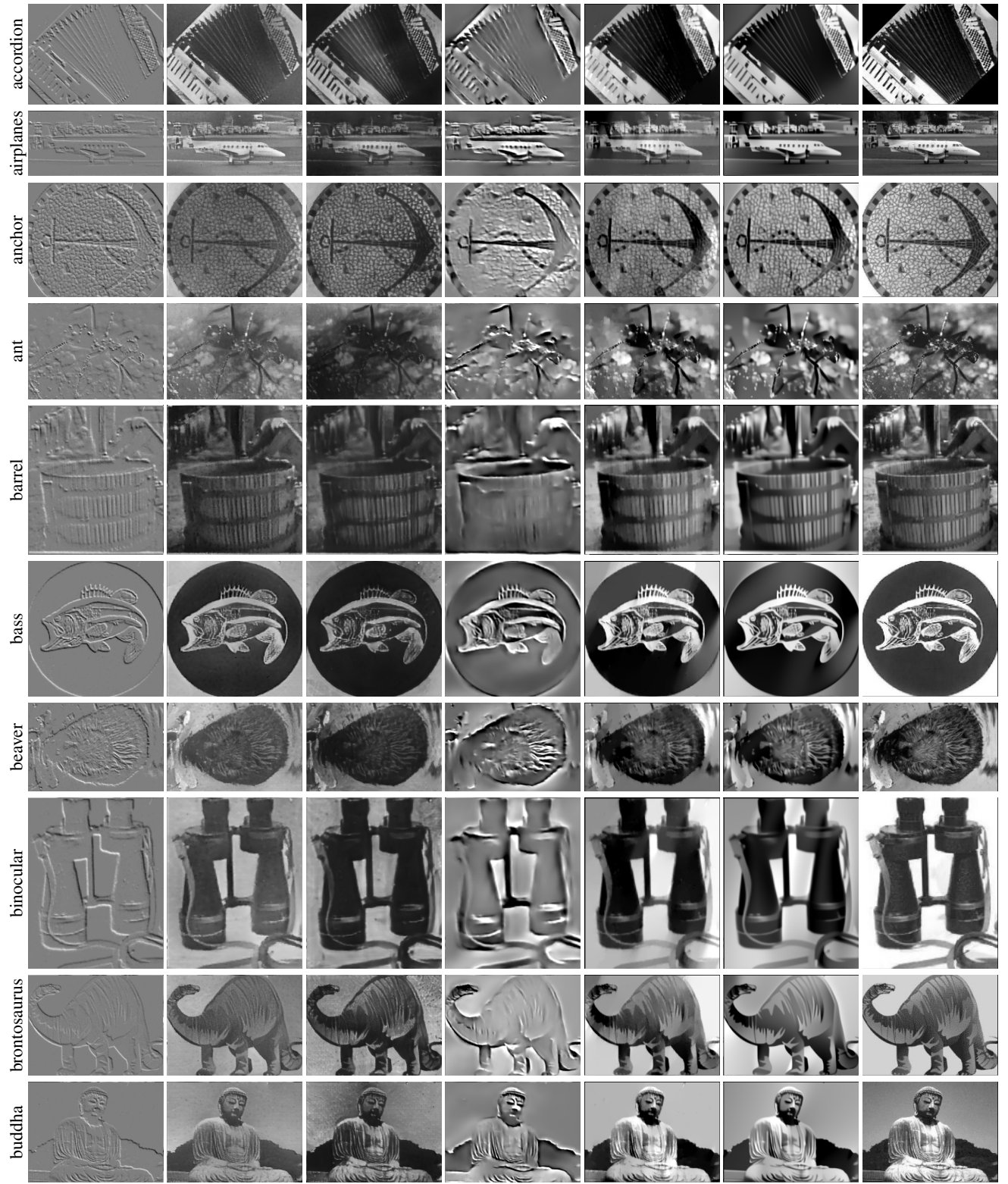
Sequence name	MSE ↓						SSIM ↑						LPIPS ↓					
	E2VID	ECNN	BTEB	Ours			E2VID	ECNN	BTEB	Ours			E2VID	ECNN	BTEB	Ours		
				Tikh.	TV	CNN				Tikh.	TV	CNN				Tikh.	TV	CNN
boxes_rotation	0.075	<b>0.039</b>	0.091	0.101	0.102	<u>0.073</u>	0.449	<b>0.510</b>	0.432	0.455	0.463	<u>0.509</u>	<u>0.400</u>	<b>0.377</b>	0.445	0.405	0.411	0.443
poster_rotation	0.115	<b>0.026</b>	0.124	0.117	0.119	<u>0.091</u>	0.391	<b>0.530</b>	0.370	0.455	0.457	<u>0.487</u>	<u>0.375</u>	<b>0.361</b>	0.463	0.419	0.429	0.438
dynamic_rotation	0.174	<b>0.074</b>	0.167	0.138	0.158	<u>0.132</u>	0.313	<u>0.397</u>	0.308	<b>0.397</b>	0.379	0.396	0.518	<b>0.476</b>	0.582	0.500	0.498	<u>0.490</u>
shapes_rotation	0.027	<b>0.014</b>	0.051	0.023	0.044	<u>0.022</u>	0.758	0.756	0.648	0.757	<u>0.801</u>	<b>0.807</b>	0.444	0.455	0.600	<u>0.438</u>	0.441	<b>0.413</b>
slider_far	0.097	<b>0.029</b>	0.096	0.120	0.094	<u>0.068</u>	0.326	<u>0.381</u>	0.327	0.283	0.330	<b>0.392</b>	<u>0.407</u>	<b>0.373</b>	0.469	0.454	0.447	0.459
slider_close	<b>0.043</b>	0.084	0.081	0.099	0.083	<u>0.073</u>	<u>0.488</u>	0.425	0.422	0.443	0.468	<b>0.522</b>	0.501	<b>0.489</b>	0.523	0.513	0.503	<u>0.496</u>
Average	0.089	<b>0.044</b>	0.102	0.100	0.100	<u>0.076</u>	0.454	<u>0.500</u>	0.418	0.465	0.483	<b>0.519</b>	<u>0.441</u>	<b>0.422</b>	0.514	0.455	0.455	0.457

Table 3. Quantitative evaluation of our method and state-of-the-art methods on sequences from [14]. We report median values of MSE, SSIM and LPIPS, since they are more robust to outliers than the mean. Images are not histogram-equalized before computing the metrics.

Sequence name	MSE ↓						SSIM ↑						LPIPS ↓					
	E2VID	ECNN	BTEB	Ours			E2VID	ECNN	BTEB	Ours			E2VID	ECNN	BTEB	Ours		
				Tikh.	TV	CNN				Tikh.	TV	CNN				Tikh.	TV	CNN
accordion	0.059	<b>0.041</b>	0.092	0.054	0.046	<u>0.044</u>	0.465	0.439	0.273	0.529	<b>0.538</b>	<u>0.530</u>	<b>0.361</b>	<u>0.378</u>	0.492	0.375	0.392	0.411
airplanes	0.044	<b>0.033</b>	0.095	0.087	<u>0.044</u>	0.046	0.489	0.434	0.359	0.550	<b>0.638</b>	<u>0.618</u>	<u>0.401</u>	0.418	0.494	0.424	<b>0.384</b>	0.408
anchor	<b>0.079</b>	<u>0.080</u>	0.145	0.112	0.083	0.106	0.351	0.293	0.332	0.460	<b>0.497</b>	<u>0.476</u>	<u>0.463</u>	<b>0.462</b>	0.562	0.496	0.466	0.514
ant	0.068	<u>0.055</u>	0.102	0.070	<b>0.055</b>	0.065	0.372	0.390	0.293	0.446	<b>0.487</b>	<u>0.447</u>	<u>0.433</u>	<b>0.429</b>	0.562	0.454	0.459	0.524
barrel	0.048	0.044	0.090	0.061	<u>0.042</u>	<b>0.041</b>	0.400	0.394	0.302	0.537	<b>0.555</b>	<u>0.551</u>	<b>0.361</b>	<u>0.370</u>	0.502	0.394	0.378	0.433
bass	0.063	<b>0.036</b>	0.087	0.060	0.049	<u>0.048</u>	0.380	0.390	0.327	0.503	<u>0.529</u>	<b>0.543</b>	<u>0.444</u>	<b>0.436</b>	0.554	0.454	0.462	0.479
beaver	0.060	<u>0.042</u>	0.077	0.056	<b>0.035</b>	0.043	0.449	0.465	0.330	<u>0.598</u>	<b>0.620</b>	0.596	<u>0.398</u>	0.406	0.535	<b>0.396</b>	0.400	0.487
binocular	<u>0.032</u>	<b>0.028</b>	0.078	0.061	0.039	0.038	0.443	0.437	0.332	0.534	<b>0.573</b>	<u>0.539</u>	0.426	<b>0.410</b>	0.509	0.427	<u>0.415</u>	0.451
bonsai	0.056	<u>0.041</u>	0.099	0.060	0.043	<b>0.039</b>	0.418	0.380	0.309	0.554	<b>0.579</b>	<u>0.573</u>	<b>0.415</b>	0.459	0.553	0.434	<u>0.415</u>	0.489
brain	0.105	0.074	0.138	0.077	<b>0.062</b>	<u>0.070</u>	0.392	0.403	0.245	0.537	<b>0.571</b>	<u>0.549</u>	0.437	0.414	0.528	<b>0.372</b>	<u>0.374</u>	0.382
brontosaurus	0.055	<b>0.042</b>	0.105	0.066	<u>0.051</u>	0.055	0.406	0.387	0.324	<u>0.520</u>	<b>0.544</b>	0.519	<b>0.412</b>	0.434	0.540	0.436	<u>0.432</u>	0.497
buddha	<u>0.050</u>	<b>0.040</b>	0.102	0.060	0.053	0.052	0.393	0.351	0.282	<u>0.542</u>	<b>0.552</b>	0.531	<b>0.418</b>	0.447	0.533	0.434	<u>0.428</u>	0.437
butterfly	0.053	0.056	0.088	0.061	<u>0.051</u>	<b>0.048</b>	0.446	0.403	0.331	0.554	<b>0.594</b>	<u>0.582</u>	0.408	<u>0.395</u>	0.516	0.417	<b>0.380</b>	0.432
camera	<u>0.032</u>	<b>0.028</b>	0.081	0.064	0.039	0.047	0.472	0.454	0.311	0.546	<b>0.585</b>	<u>0.574</u>	<b>0.362</b>	0.370	0.489	0.394	0.365	<u>0.364</u>
cannon	0.045	<b>0.036</b>	0.088	0.055	0.042	<u>0.041</u>	0.504	0.461	0.332	0.571	<b>0.600</b>	<u>0.589</u>	<b>0.357</b>	<u>0.392</u>	0.501	0.403	0.396	0.417
car_side	0.050	0.051	0.070	0.044	<b>0.033</b>	<u>0.039</u>	0.460	0.406	0.330	0.569	<b>0.590</b>	<u>0.585</u>	<b>0.397</b>	<u>0.398</u>	0.513	0.421	0.406	0.436
ceiling_fan	0.081	<b>0.058</b>	0.108	0.093	<u>0.067</u>	0.074	0.338	0.255	0.326	0.441	<b>0.527</b>	<u>0.518</u>	<u>0.500</u>	<b>0.484</b>	0.544	0.511	0.508	0.504
cellphone	<b>0.050</b>	<u>0.053</u>	0.082	0.065	0.067	0.064	0.367	0.283	0.312	0.496	<b>0.523</b>	<u>0.514</u>	0.434	0.461	0.527	<u>0.433</u>	<b>0.419</b>	0.451
chair	0.060	0.063	0.104	0.066	<b>0.049</b>	<u>0.058</u>	0.376	0.338	0.317	0.508	<b>0.571</b>	<u>0.542</u>	<b>0.379</b>	<u>0.407</u>	0.510	0.409	0.409	0.435
chandelier	0.081	0.059	0.103	<u>0.053</u>	0.056	<b>0.041</b>	0.372	0.387	0.301	<u>0.577</u>	0.569	<b>0.599</b>	0.441	0.451	0.519	<b>0.404</b>	<u>0.426</u>	0.455
cougar	0.062	<u>0.044</u>	0.092	0.055	0.053	<b>0.043</b>	0.384	0.384	0.296	<u>0.554</u>	<b>0.569</b>	0.517	<b>0.402</b>	<u>0.411</u>	0.538	0.413	0.451	0.506
crab	<u>0.049</u>	<b>0.044</b>	0.099	0.065	0.049	0.051	0.463	0.424	0.308	<b>0.556</b>	<u>0.554</u>	0.548	<u>0.396</u>	<b>0.396</b>	0.537	0.427	0.423	0.480
crayfish	0.058	<b>0.044</b>	0.095	0.072	<u>0.056</u>	0.068	0.399	0.348	0.291	0.433	<u>0.472</u>	<b>0.483</b>	<b>0.421</b>	<u>0.446</u>	0.553	0.487	0.493	0.539
crocodile	0.077	0.064	0.095	0.049	<u>0.046</u>	<b>0.044</b>	0.399	0.409	0.271	<u>0.584</u>	<b>0.590</b>	0.570	<b>0.407</b>	0.438	0.571	<u>0.420</u>	0.433	0.504
cup	0.054	0.049	0.090	0.057	<b>0.034</b>	<u>0.045</u>	0.387	0.359	0.285	0.459	<u>0.513</u>	<b>0.523</b>	0.479	0.465	0.547	<u>0.457</u>	<b>0.453</b>	0.460
dalmatian	0.045	0.037	0.076	0.043	<b>0.030</b>	<u>0.032</u>	0.508	0.482	0.366	0.578	<b>0.634</b>	<u>0.608</u>	<u>0.393</u>	0.413	0.503	0.407	<b>0.379</b>	0.421
dollar_bill	0.040	<b>0.030</b>	0.072	0.047	0.043	<u>0.037</u>	0.526	0.509	0.371	<u>0.626</u>	<b>0.648</b>	0.624	<u>0.309</u>	0.332	0.452	0.318	<b>0.306</b>	0.385
dolphin	0.085	0.071	0.091	0.062	<u>0.062</u>	<b>0.057</b>	0.342	0.330	0.279	<u>0.460</u>	<b>0.472</b>	0.434	<u>0.447</u>	<b>0.446</b>	0.536	0.462	0.466	0.520
dragonfly	0.100	<b>0.071</b>	0.134	0.092	<u>0.086</u>	0.094	0.314	0.303	0.270	0.471	<u>0.478</u>	<b>0.483</b>	<b>0.449</b>	0.466	0.554	0.475	<u>0.452</u>	0.512

Table 4. Quantitative evaluation of our method and state-of-the-art methods on sequences from N-Caltech [37]. We report median values of MSE, SSIM and LPIPS, since they are more robust to outliers than the mean. Images are histogram-equalized before computing the metrics.





(a) NIWE (events) (b) E2VID [7] (c) ECNN [20] (d) BTB [26] (e) Ours (TV) (f) Ours (CNN) (g) Ground truth

Figure 9. Qualitative comparison of our method with the state of the art on sequences from [37]. Histogram equalization is not used.

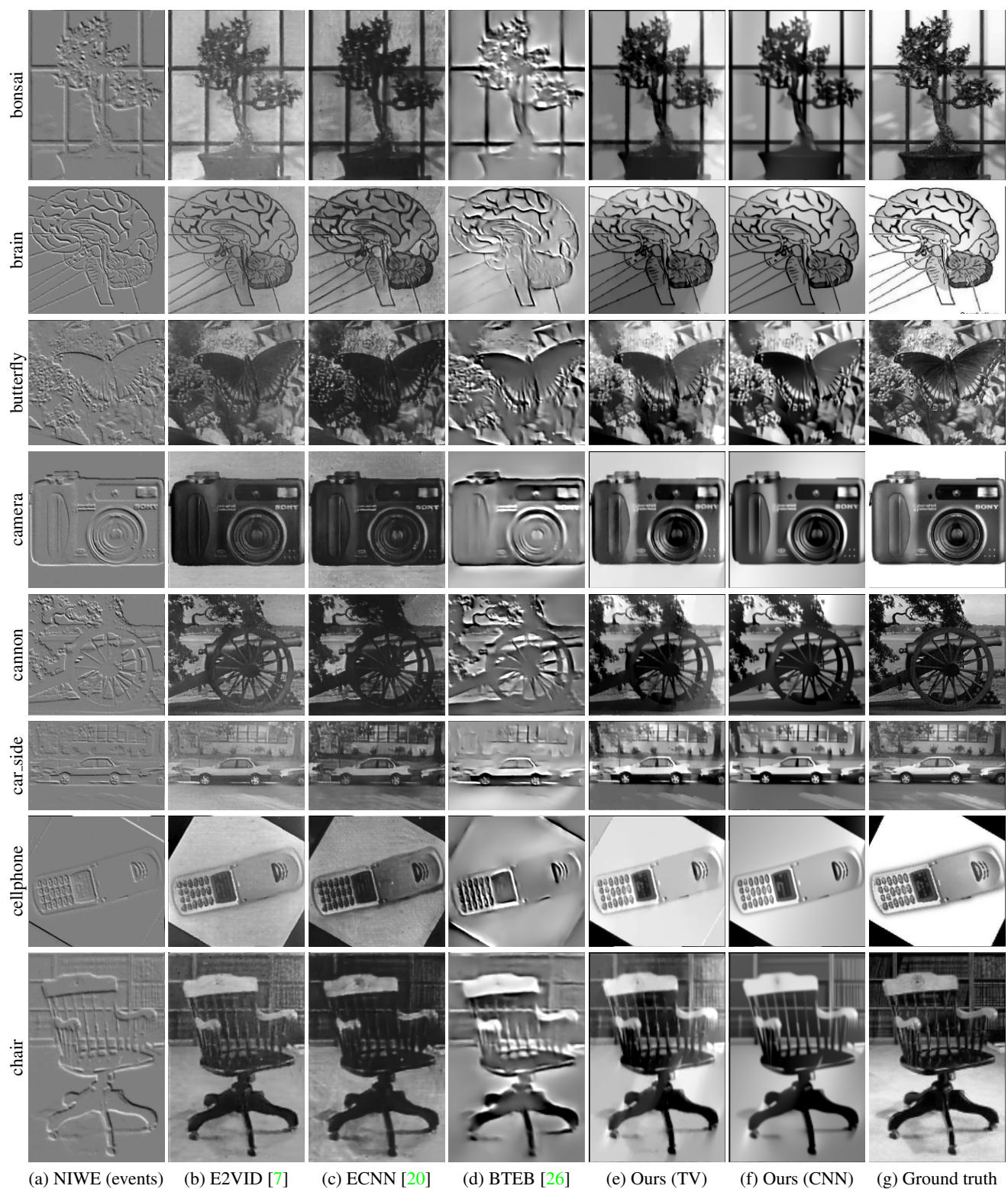


Figure 10. Continuation of Fig. 9.



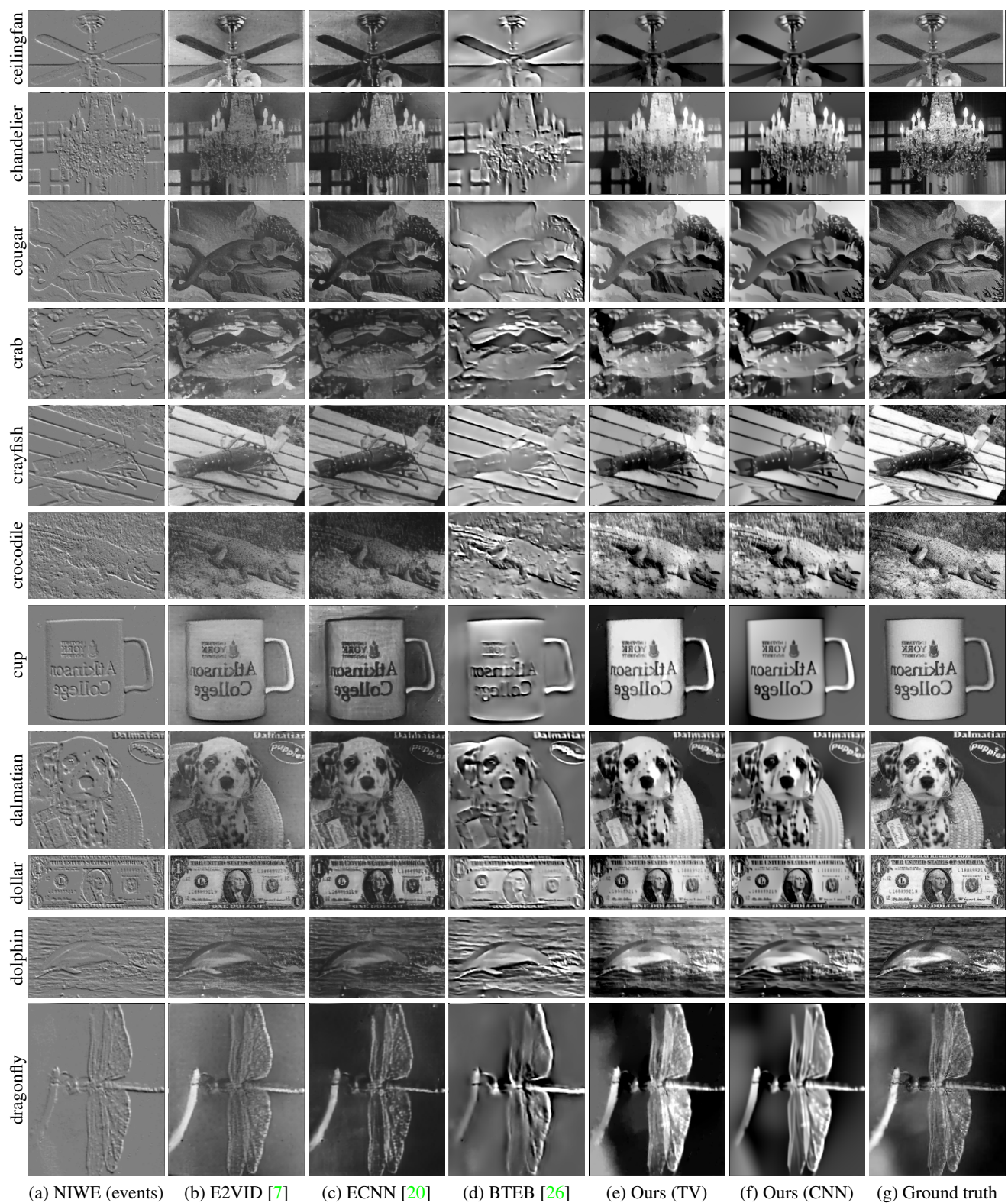


Figure 11. Continuation of Fig. 10.



Sequence name	MSE ↓						SSIM ↑						LPIPS ↓					
				Ours						Ours						Ours		
	E2VID	ECNN	BTEB	Tikh.	TV	CNN	E2VID	ECNN	BTEB	Tikh.	TV	CNN	E2VID	ECNN	BTEB	Tikh.	TV	CNN
accordion	0.050	0.037	0.090	0.045	<u>0.037</u>	<b>0.033</b>	0.463	0.462	0.321	0.581	<u>0.603</u>	<b>0.633</b>	<u>0.336</u>	0.354	0.461	0.346	<b>0.328</b>	0.372
airplanes	<b>0.031</b>	0.055	0.058	0.071	0.039	<u>0.036</u>	0.677	0.558	0.541	0.695	<u>0.764</u>	<b>0.775</b>	<u>0.334</u>	0.387	0.458	0.394	<b>0.329</b>	0.372
anchor	0.062	0.093	0.080	0.082	<b>0.049</b>	<u>0.052</u>	0.652	0.525	0.595	0.676	<u>0.747</u>	<b>0.778</b>	<u>0.376</u>	0.407	0.467	0.411	<b>0.358</b>	0.395
ant	0.041	0.044	0.059	0.040	<b>0.028</b>	<u>0.033</u>	0.618	0.514	0.477	0.667	<b>0.715</b>	<u>0.709</u>	<u>0.373</u>	0.390	0.490	0.390	<b>0.349</b>	0.405
barrel	0.035	0.044	0.066	0.036	<u>0.032</u>	<b>0.032</b>	0.568	0.518	0.394	0.661	<b>0.698</b>	<u>0.662</u>	<u>0.325</u>	0.343	0.472	0.342	<b>0.323</b>	0.401
bass	0.034	<u>0.029</u>	0.052	0.040	<b>0.026</b>	0.029	0.572	0.566	0.459	<u>0.674</u>	<b>0.683</b>	0.661	0.394	<u>0.392</u>	0.491	0.411	<b>0.372</b>	0.425
beaver	0.032	0.044	0.048	0.039	<b>0.024</b>	<u>0.027</u>	0.567	0.508	0.409	<u>0.681</u>	<b>0.715</b>	0.678	<u>0.371</u>	0.389	0.511	0.376	<b>0.355</b>	0.421
binocular	<u>0.036</u>	0.066	0.086	0.055	0.044	<b>0.035</b>	0.639	0.553	0.464	0.658	<u>0.708</u>	<b>0.714</b>	0.369	0.374	0.483	<u>0.361</u>	<b>0.306</b>	0.361
bonsai	0.063	0.062	0.070	0.067	<b>0.046</b>	<u>0.046</u>	0.538	0.454	0.438	0.624	<b>0.719</b>	<u>0.650</u>	<u>0.393</u>	0.435	0.516	0.405	<b>0.352</b>	0.432
brain	0.064	0.061	0.092	0.096	<u>0.055</u>	<b>0.043</b>	0.438	0.365	0.332	0.531	<b>0.593</b>	<u>0.580</u>	0.392	0.378	0.458	0.345	<b>0.296</b>	<u>0.325</u>
brontosaurus	0.038	0.047	0.063	0.039	<b>0.031</b>	<u>0.036</u>	0.598	0.498	0.496	0.681	<b>0.708</b>	<u>0.683</u>	<u>0.377</u>	0.410	0.500	0.398	<b>0.364</b>	0.446
buddha	0.070	0.081	0.071	0.063	<b>0.038</b>	<u>0.039</u>	0.580	0.483	0.470	0.628	<b>0.732</b>	<u>0.693</u>	<u>0.394</u>	0.418	0.503	0.402	<b>0.359</b>	0.414
butterfly	0.048	0.045	0.066	0.049	<b>0.033</b>	<u>0.038</u>	0.654	0.562	0.503	0.689	<b>0.724</b>	<u>0.718</u>	0.351	0.374	0.443	<u>0.341</u>	<b>0.322</b>	0.372
camera	0.049	0.090	0.075	0.068	<b>0.036</b>	<u>0.046</u>	0.637	0.520	0.465	0.666	<b>0.725</b>	<u>0.718</u>	0.335	0.340	0.426	0.338	<b>0.280</b>	<u>0.317</u>
cannon	<b>0.029</b>	0.047	0.065	0.038	0.034	<u>0.029</u>	0.621	0.530	0.465	0.671	<b>0.711</b>	<u>0.702</u>	<u>0.330</u>	0.359	0.472	0.371	<b>0.317</b>	0.361
car_side	0.035	0.024	0.042	0.023	<u>0.021</u>	<b>0.018</b>	0.659	0.604	0.519	0.723	<b>0.767</b>	<u>0.748</u>	0.372	<u>0.371</u>	0.506	0.411	<b>0.362</b>	0.410
ceiling_fan	<b>0.035</b>	0.039	0.057	0.038	0.047	<u>0.036</u>	0.681	0.526	0.610	0.697	<u>0.734</u>	<b>0.738</b>	0.407	0.439	0.451	0.423	<u>0.387</u>	<b>0.384</b>
cellphone	0.057	0.066	0.092	0.066	<b>0.052</b>	<u>0.056</u>	0.537	0.472	0.456	0.617	<b>0.653</b>	<u>0.650</u>	0.395	0.399	0.477	0.382	<b>0.336</b>	<u>0.379</u>
chair	0.036	0.074	0.067	0.048	<b>0.030</b>	<u>0.033</u>	0.672	0.514	0.562	0.704	<u>0.745</u>	<b>0.757</b>	0.327	0.384	0.444	0.366	<b>0.295</b>	<u>0.324</u>
chandelier	0.052	0.037	0.065	0.040	<u>0.032</u>	<b>0.025</b>	0.562	0.494	0.443	0.684	<b>0.736</b>	<u>0.714</u>	0.377	0.396	0.488	0.364	<b>0.320</b>	<u>0.360</u>
cougar	<u>0.033</u>	0.034	0.049	0.034	0.043	<b>0.029</b>	0.556	0.529	0.438	<u>0.651</u>	<b>0.666</b>	0.630	<b>0.380</b>	0.407	0.531	<u>0.406</u>	0.413	0.481
crab	0.043	0.046	0.064	0.039	<u>0.035</u>	<b>0.030</b>	0.559	0.523	0.423	0.673	<b>0.697</b>	<u>0.681</u>	<b>0.372</b>	0.396	0.523	0.398	<u>0.383</u>	0.411
crayfish	0.044	0.073	0.060	0.057	<b>0.037</b>	<u>0.044</u>	0.623	0.502	0.540	0.682	<u>0.716</u>	<b>0.723</b>	<u>0.378</u>	0.403	0.489	0.410	<b>0.368</b>	0.416
crocodile	0.042	0.034	0.057	0.035	<u>0.031</u>	<b>0.027</b>	0.548	0.518	0.432	<u>0.671</u>	<b>0.678</b>	0.651	<b>0.378</b>	0.431	0.530	0.414	<u>0.410</u>	0.497
cup	0.046	0.054	0.057	0.053	<b>0.028</b>	<u>0.034</u>	0.662	0.544	0.540	0.671	<b>0.750</b>	<u>0.734</u>	0.383	0.419	0.455	0.404	<b>0.367</b>	<u>0.373</u>
dalmatian	0.031	0.036	0.042	0.030	<u>0.025</u>	<b>0.020</b>	0.691	0.617	0.543	0.703	<b>0.769</b>	<u>0.742</u>	<u>0.333</u>	0.335	0.457	0.360	<b>0.313</b>	0.348
dollar_bill	<u>0.037</u>	0.092	0.047	0.049	0.042	<b>0.035</b>	0.572	0.495	0.450	0.669	<b>0.702</b>	<u>0.694</u>	0.295	0.345	0.463	<u>0.291</u>	<b>0.286</b>	0.360
dolphin	0.042	<b>0.025</b>	0.048	0.040	0.045	<u>0.035</u>	0.597	0.536	0.510	<u>0.658</u>	<b>0.663</b>	0.647	<b>0.381</b>	<u>0.393</u>	0.478	0.428	0.412	0.444
dragonfly	0.081	0.066	0.058	0.068	<b>0.046</b>	<u>0.046</u>	0.629	0.512	0.567	0.670	<b>0.706</b>	<u>0.701</u>	<b>0.378</b>	0.417	0.486	0.414	<u>0.382</u>	0.429

Table 5. Quantitative evaluation of our method and state-of-the-art methods on sequences from N-Caltech [37]. We report median values of MSE, SSIM and LPIPS, since they are more robust to outliers than the mean. Images are not histogram-equalized before computing the metrics.



Figure 12. Evolution of the solution  $(\ell_k, \mathbf{z}_k)$  in the alternating, iterative solver (12). We start  $\ell_0$  from the solution provided by the total variation (TV). As iterations proceed,  $\mathbf{z}_k$  is refined, capturing more fine details, becoming less smooth. *The first column contains animations if opened with Acrobat Reader, with the iteration counter in red. Please click on the images if they do not play automatically. Event data from [14].*

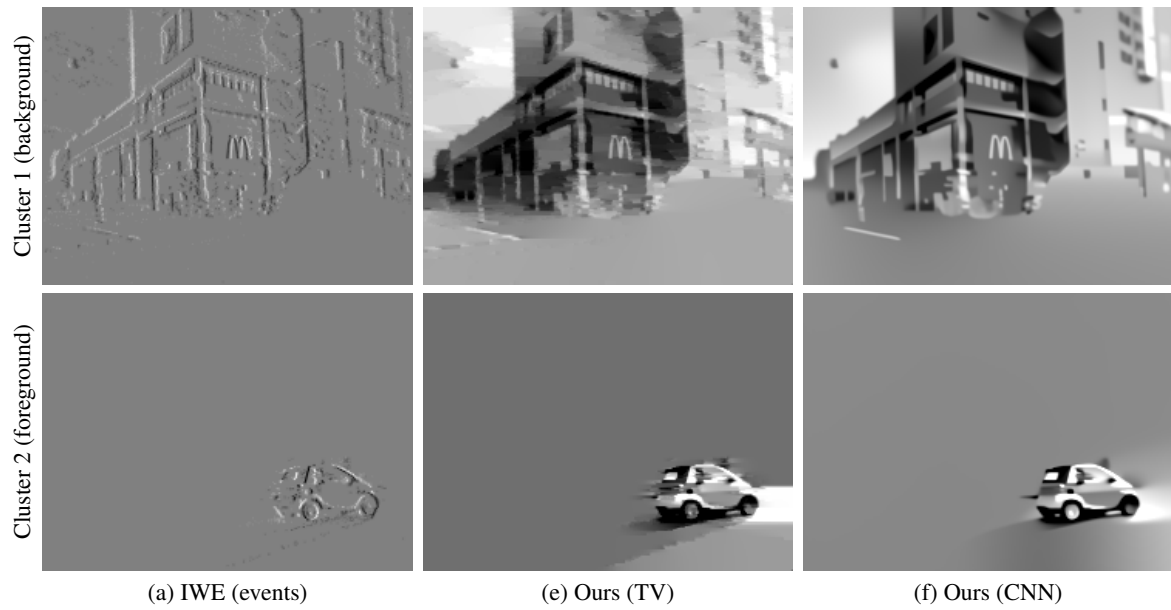


Figure 13. Image reconstruction after event-based motion segmentation. The scene consists of a moving car on a street while the camera is panning. The majority of events are due to the apparent motion of the static parts of the scene (e.g., buildings) as the camera moves (cluster 1). The car, segmented in a separate cluster as an independent moving object with respect to the background, produces fewer events. Our image reconstruction method can be applied to each cluster independently, i.e., to the IWE produced by each cluster. Event data from [41].



## References

- [1] Patrick Lichtsteiner, Christoph Posch, and Tobi Delbruck, “A 128x128 120dB 30mW asynchronous vision sensor that responds to relative intensity change,” in *IEEE Intl. Solid-State Circuits Conf. (ISSCC)*, pp. 2060–2069, 2006.
- [2] Guillermo Gallego, Tobi Delbruck, Garrick Orchard, Chiara Bartolozzi, Brian Taba, Andrea Censi, Stefan Leutenegger, Andrew Davison, Jörg Conradt, Kostas Daniilidis, and Davide Scaramuzza, “Event-based vision: A survey,” *IEEE Trans. Pattern Anal. Mach. Intell.*, 2020.
- [3] Guang Chen, Hu Cao, Jorg Conradt, Huajin Tang, Florian Rohrbach, and Alois Knoll, “Event-based neuromorphic vision for autonomous driving: A paradigm shift for bio-inspired visual sensing and perception,” *IEEE Signal Process. Mag.*, vol. 37, no. 4, pp. 34–49, 2020.
- [4] Hanme Kim, Ankur Handa, Ryad Benosman, Sio-Hoi Ieng, and Andrew J. Davison, “Simultaneous mosaicing and tracking with an event camera,” in *British Mach. Vis. Conf. (BMVC)*, 2014.
- [5] Gottfried Munda, Christian Reinbacher, and Thomas Pock, “Real-time intensity-image reconstruction for event cameras using manifold regularisation,” *Int. J. Comput. Vis.*, vol. 126, pp. 1381–1393, July 2018.
- [6] Cedric Scheerlinck, Nick Barnes, and Robert Mahony, “Continuous-time intensity estimation using event cameras,” in *Asian Conf. Comput. Vis. (ACCV)*, 2018.
- [7] Henri Rebecq, René Ranftl, Vladlen Koltun, and Davide Scaramuzza, “High speed and high dynamic range video with an event camera,” *IEEE Trans. Pattern Anal. Mach. Intell.*, 2019.
- [8] S.M. Mostafavi I., Lin Wang, and Kuk-Jin Yoon Yoon, “Learning to reconstruct hdr images from events, with applications to depth and flow prediction,” *Int. J. Comput. Vis.*, vol. 129, pp. 900–920, Apr. 2021.
- [9] Richard Hartley and Andrew Zisserman, *Multiple View Geometry in Computer Vision*. Cambridge University Press, 2003. 2nd Edition.
- [10] Patrick Lichtsteiner, Christoph Posch, and Tobi Delbruck, “A 128x128 120 dB 15  $\mu$ s latency asynchronous temporal contrast vision sensor,” *IEEE J. Solid-State Circuits*, vol. 43, no. 2, pp. 566–576, 2008.
- [11] Bongki Son, Yunjae Suh, Sungho Kim, Heejae Jung, Jun-Seok Kim, Changwoo Shin, Keunju Park, Kyoobin Lee, Jinman Park, Jooyeon Woo, Yohan Roh, Hyunku Lee, Yibing Wang, Ilia Ovsianikov, and Hyunsurk Ryu, “A 640x480 dynamic vision sensor with a 9 $\mu$ m pixel and 300Meps address-event representation,” in *IEEE Intl. Solid-State Circuits Conf. (ISSCC)*, 2017.
- [12] Yunjae Suh, Seungnam Choi, Masamichi Ito, Jeongseok Kim, Youngho Lee, Jongseok Seo, Heejae Jung, Dong-Hee Yeo, Seol Namgung, Jongwoo Bong, Jun seok Kim, Paul K. J. Park, Joonseok Kim, Hyunsurk Ryu, and Yongin Park, “A 1280x960 Dynamic Vision Sensor with a 4.95- $\mu$ m pixel pitch and motion artifact minimization,” in *IEEE Int. Symp. Circuits Syst. (ISCAS)*, 2020.
- [13] Thomas Finateu, Atsumi Niwa, Daniel Matolin, Koya Tsuchimoto, Andrea Mascheroni, Etienne Reynaud, Poo-ria Mostafalu, Frederick Brady, Ludovic Chotard, Florian LeGoff, Hirotsugu Takahashi, Hayato Wakabayashi, Yusuke Oike, and Christoph Posch, “A 1280x720 back-illuminated stacked temporal contrast event-based vision sensor with 4.86 $\mu$ m pixels, 1.066geps readout, programmable event-rate controller and compressive data-formatting pipeline,” in *IEEE Intl. Solid-State Circuits Conf. (ISSCC)*, 2020.
- [14] Elias Mueggler, Henri Rebecq, Guillermo Gallego, Tobi Delbruck, and Davide Scaramuzza, “The event-camera dataset and simulator: Event-based data for pose estimation, visual odometry, and SLAM,” *Int. J. Robot. Research*, vol. 36, no. 2, pp. 142–149, 2017.
- [15] Matthew Cook, Luca Gugelmann, Florian Jug, Christoph Krautz, and Angelika Steger, “Interacting maps for fast visual interpretation,” in *Int. Joint Conf. Neural Netw. (IJCNN)*, pp. 770–776, 2011.
- [16] Hanme Kim, Stefan Leutenegger, and Andrew J. Davison, “Real-time 3D reconstruction and 6-DoF tracking with an event camera,” in *Eur. Conf. Comput. Vis. (ECCV)*, pp. 349–364, 2016.
- [17] Henri Rebecq, Timo Horstschäfer, Guillermo Gallego, and Davide Scaramuzza, “EVO: A geometric approach to event-based 6-DOF parallel tracking and mapping in real-time,” *IEEE Robot. Autom. Lett.*, vol. 2, no. 2, pp. 593–600, 2017.
- [18] Patrick Bardow, Andrew J. Davison, and Stefan Leutenegger, “Simultaneous optical flow and intensity estimation from an event camera,” in *IEEE Conf. Comput. Vis. Pattern Recog. (CVPR)*, pp. 884–892, 2016.
- [19] Cedric Scheerlinck, Henri Rebecq, Daniel Gehrig, Nick Barnes, Robert Mahony, and Davide Scaramuzza, “Fast image reconstruction with an event camera,” in *IEEE Winter Conf. Appl. Comput. Vis. (WACV)*, 2020.
- [20] Timo Stoffregen, Cedric Scheerlinck, Davide Scaramuzza, Tom Drummond, Nick Barnes, Lindsay Kleeman, and Robert Mahony, “Reducing the sim-to-real gap for event cameras,” in *Eur. Conf. Comput. Vis. (ECCV)*, 2020.
- [21] Patrick Bardow, *Estimating General Motion and Intensity from Event Cameras*. PhD thesis, Imperial College London, Department of Computing, 2018.
- [22] Souptik Barua, Yoshitaka Miyatani, and Ashok Veeraraghavan, “Direct face detection and video reconstruction from event cameras,” in *IEEE Winter Conf. Appl. Comput. Vis. (WACV)*, pp. 1–9, 2016.
- [23] Hadar Cohen-Duwek, Albert Shalumov, and Elishai Ezra Tsur, “Image reconstruction from neuromorphic event cameras using laplacian-prediction and poisson integration with spiking and artificial neural networks,” in *IEEE Conf. Comput. Vis. Pattern Recog. Workshops (CVPRW)*, pp. 1333–1341, 2021.
- [24] Lin Wang, Tae-Kyun Kim, and Kuk-Jin Yoon, “EventSR: From asynchronous events to image reconstruction, restoration, and super-resolution via end-to-end adversarial learning,” in *IEEE Conf. Comput. Vis. Pattern Recog. (CVPR)*, 2020.
- [25] Song Zhang, Yu Zhang, Zhe Jiang, Dongqing Zou, Jimmy Ren, and Bin Zhou, “Learning to see in the dark with events,” in *Eur. Conf. Comput. Vis. (ECCV)*, pp. 666–682, 2020.

- [26] Federico Paredes-Valles and Guido C. H. E. de Croon, “Back to event basics: Self-supervised learning of image reconstruction for event cameras via photometric constancy,” in *IEEE Conf. Comput. Vis. Pattern Recog. (CVPR)*, pp. 3446–3455, 2021.
- [27] Alex Zihao Zhu, Liangzhe Yuan, Kenneth Chaney, and Kostas Daniilidis, “Unsupervised event-based learning of optical flow, depth, and egomotion,” in *IEEE Conf. Comput. Vis. Pattern Recog. (CVPR)*, 2019.
- [28] Yunhao Zou, Yinqiang Zheng, Tsuyoshi Takatani, and Ying Fu, “Learning to reconstruct high speed and high dynamic range videos from events,” in *IEEE Conf. Comput. Vis. Pattern Recog. (CVPR)*, pp. 2024–2033, 2021.
- [29] Guillermo Gallego, Henri Rebecq, and Davide Scaramuzza, “A unifying contrast maximization framework for event cameras, with applications to motion, depth, and optical flow estimation,” in *IEEE Conf. Comput. Vis. Pattern Recog. (CVPR)*, pp. 3867–3876, 2018.
- [30] A.N. Tikhonov, A. Goncharsky, V.V. Stepanov, and A.G. Yagola, *Numerical Methods for the Solution of Ill-Posed Problems*. Mathematics and Its Applications, Springer Netherlands, 1995.
- [31] Leonid I. Rudin, Stanley Osher, and Emad Fatemi, “Nonlinear total variation based noise removal algorithms,” *Physica D: Nonlinear Phenomena*, vol. 60, pp. 259–268, Nov. 1992.
- [32] Minas Benyamin, Jeff Calder, Ganesh Sundaramoorthi, and Anthony J. Yezzi, “Accelerated variational pdes for efficient solution of regularized inversion problems,” *J. Math. Imaging Vis.*, vol. 62, no. 1, pp. 10–36, 2020.
- [33] Kai Zhang, Yawei Li, Wangmeng Zuo, Lei Zhang, Luc Van Gool, and Radu Timofte, “Plug-and-play image restoration with deep denoiser prior,” *IEEE Trans. Pattern Anal. Mach. Intell.*, 2021.
- [34] Kai Zhang, Wangmeng Zuo, Shuhang Gu, and Lei Zhang, “Learning deep cnn denoiser prior for image restoration,” in *IEEE Conf. Comput. Vis. Pattern Recog. (CVPR)*, pp. 3929–3938, 2017.
- [35] Kostadin Dabov, Alessandro Foi, Vladimir Katkovnik, and Karen Egiazarian, “Color image denoising via sparse 3d collaborative filtering with grouping constraint in luminance-chrominance space,” in *IEEE Int. Conf. Image Process. (ICIP)*, vol. 1, pp. I–313, 2007.
- [36] Guillermo Gallego and Davide Scaramuzza, “Accurate angular velocity estimation with an event camera,” *IEEE Robot. Autom. Lett.*, vol. 2, no. 2, pp. 632–639, 2017.
- [37] Garrick Orchard, Ajinkya Jayawant, Gregory K. Cohen, and Nitish Thakor, “Converting static image datasets to spiking neuromorphic datasets using saccades,” *Front. Neurosci.*, vol. 9, p. 437, 2015.
- [38] Zhou Wang, Alan C. Bovik, Hamid R. Sheikh, and Eero P. Simoncelli, “Image quality assessment: From error visibility to structural similarity,” *IEEE Trans. Image Process.*, vol. 13, pp. 600–612, Apr. 2004.
- [39] Richard Zhang, Phillip Isola, Alexei A. Efros, Eli Shechtman, and Oliver Wang, “The unreasonable effectiveness of deep features as a perceptual metric,” in *IEEE Conf. Comput. Vis. Pattern Recog. (CVPR)*, 2018.
- [40] Mathias Gehrig, Mario Millhäusler, Daniel Gehrig, and Davide Scaramuzza, “E-RAFT: Dense optical flow from event cameras,” in *3D Vision (3DV)*, 2021.
- [41] Timo Stofregen, Guillermo Gallego, Tom Drummond, Lindsay Kleeman, and Davide Scaramuzza, “Event-based motion segmentation by motion compensation,” in *Int. Conf. Comput. Vis. (ICCV)*, pp. 7243–7252, 2019.
- [42] Yi Zhou, Guillermo Gallego, Xiuyuan Lu, Siqi Liu, and Shaojie Shen, “Event-based motion segmentation with spatio-temporal graph cuts,” *IEEE Trans. Neural Netw. Learn. Syst.*, 2021.